9-8-2011

Using Borehole Logging and Electron Backscatter Diffraction to Orient an Ice Core from Upper Fremont Glacier, Wyoming, USA

R. W. Obbard
Dartmouth College

T. Cassano
Dartmouth College

K. Aho
Dartmouth College

G. Troderman
Dartmouth College

I. Baker
Dartmouth College

Instruments and Methods

Using borehole logging and electron backscatter diffraction to orient an ice core from Upper Fremont Glacier, Wyoming, USA

R.W. OBBARD, T. CASSANO, K. AHO, G. TRODERMAN, I. BAKER

Thayer School of Engineering, Dartmouth College, Hanover, New Hampshire 03755-8000, USA
E-mail: rachel.w.obbard@dartmouth.edu

ABSTRACT. While glacier fabric reflects the accumulated strain, detailed azimuthal information is required to link the microstructure to the flow, and this is not easily gathered at depth. Borehole logging provides a way to obtain a log of azimuthal orientation of tilted stratigraphic features that can be used to orient the core with respect to glacier flow. We demonstrate this using acoustic borehole logs and the ice core from a 162 m borehole in Upper Fremont Glacier, Wind River Range, Wyoming, USA. We measured the dip of tilted dust and bubble layers in the actual ice core, identified them on the borehole log, then used their strike to orient the core sections containing them. We examined the crystal orientation fabric of our samples, using electron backscatter diffraction in a scanning electron microscope. When we compared the orientation of the tilted layers in some samples with the fabric, we found that the normal to the foliation and the *c*-axes maxima both pointed in the direction of maximum shear stress. This illustrates the usefulness of borehole logs for orienting ice cores after removal from the borehole, and for developing a better understanding of fabric development.

1. INTRODUCTION AND BACKGROUND

1.1. Introduction

Glaciers are natural archives of past climate, and ice cores are used in the development of high-resolution paleoclimate and environmental records (e.g. Mayewski and others, 1984). Temperate-zone alpine cores are useful for examining potential climatic forcing factors such as greenhouse gases and changes in solar activity, and can also provide information on changes in temperature and atmospheric circulation (e.g. Kang and others, 2002; Naftz and others, 2002). Although much information is gleaned from ice-core chemistry, an examination of microstructure is important for understanding glacier rheology and post-depositional changes. Preferred orientations in crystal orientation fabric can yield information about the state of stress and strain history that are related to glacier flow (Budd and Jacka, 1989; Thorsteinsson and others, 2003).

Foliation (layered features developed during deformation) is quite common in temperate glaciers, and is characterized by abrupt changes in ice texture (crystal size), the presence of particles and the presence and shape of bubbles (Hambrey, 1977).

Dipping layers are also observed in large polar ice sheets (e.g. Gow and Meese, 2007), and a method of using them for azimuthal orientation of cores could be quite useful. In the past, only ice that was collected manually (e.g. from a glacier surface, snout or tunnel) could be reliably oriented. For deep ice cores collected with a simple electromechanical drill and no down-hole instrumentation, azimuthal orientation was impossible to determine in situ and not typically recorded. Hence most crystal orientation data (i.e. pole figures) for core ice do not include this information. Recently, data from down-hole instrumentation have been used to orient core sections as they are removed from the hole (personal communication from K. Taylor, 2011). In related work, Roberson and Hubbard (2010) used digital optical televiewing to investigate englacial structures such as sediment layers and fractures across boreholes and to correlate these with surface maps. Their results show how borehole logging can be used to characterize englacial structures on that scale.

1.2. Crystal orientation in glaciers

Microstructure in ice from temperate glaciers, primarily studied on the lateral margins or in the ablation zone (e.g. Jonsson, 1970; Hambrey, 1976), typically has a strong fabric with two, three or four *c*-axis maxima. The number and orientation of these clusters is a function of the strain history and state of stress in that portion of the glacier.

Multiple pole fabrics can be produced by complex, three-dimensional states of stress stemming from, for example, diverging or converging flow, shear near the glacier's margins, horizontal shear stress with depth, bed irregularities, and combinations of these (Budd, 1972; Budd and Jacka, 1989). Confined vertical compression and longitudinal extension in the center of the accumulation zone, most pronounced in the upper layers, produces a two-pole fabric where the poles are 45° to the principal stresses (Budd, 1972; Kamb, 1972; Budd and Matsuda, 1974; Budd and Jacka, 1989). Changes in the state of stress during movement (e.g. stress relaxation) can also produce multiple-maxima fabric (Budd and Jacka, 1989). Multiple maxima can also reflect transition states between two fabrics (e.g. one with two maxima and one with a small circle girdle) (Budd, 1972; Budd and Jacka, 1989).

Rigsby (1951) performed crystal fabric studies on ice from surface locations on the medial moraine of the accumulation zone of Emmons Glacier (46°51′46″ N, 121°42′59″ W; 4200 m a.s.l.) on Mount Rainier, Washington, USA, and found that the normals to the foliation planes were located near the centers of four-maxima, diamond-shaped *c*-axis fabrics. Rigsby (1951) concluded that these fabrics were the

result of recrystallization of a single-maximum pattern in the presence of compression and longitudinal shear stress, where the long axis of the diamond is parallel to the stress vector acting upon the plane of maximum shear stress. In his study of temperate glaciers in northern Norway, the Swiss Alps and the Canadian Arctic, Hambrey (1976, 1977) also found fabrics composed of three or four strong maxima, although the latter did not always form a diamond. In each case, the pole to the foliation plane either coincided with one of these or fell into the center of the grouping.

1.3. Upper Fremont Glacier

Upper Fremont Glacier (UFG) (43°07′52″ N, 109°36′58″ W; 4000 m a.s.l.), Wyoming, USA, is a remote valley glacier with a thickness of 60–172 m in the accumulation zone (Naftz and Smith, 1993; Naftz and others, 2002), and has an average accumulation rate of 70 cm ice equiv. a^{-1} (Schuster and others, 2000), and a rapid densification rate producing a density of 0.85 g cm^{-3} at 14 m depth (Naftz and others, 2002). Ice velocity is 0.8–3.1 m a^{-1}. Mean surface air temperature at UFG, measured between 11 July 1990 and 10 July 1991, was –6.9°C (Naftz and others, 2002). The temperature in the ice itself (at 10 m depth) is at the pressure-melting point (0 ± 0.4°C) (Naftz and others, 2002). This may be the result of the percolation of summer surface and near-surface meltwater through the firn layer, which would warm the lower layers and produce the clear-ice bands observed in the core.

In 1991, a 160 m core was removed from UFG which provided evidence, in the ^{14}C and $\delta^{18}O$ records, that the ice at the bottom of the glacier was formed from snow which fell between AD 1716 and 1820 (Naftz and others, 1996). Later refinement using electrical conductivity measurements allowed identification of a major climatic shift to warmer temperatures at AD 1845 marking the end of the Little Ice Age (±10 years) (Schuster and others, 2000).

In 1998, a 162 m ice core (DH98-4) 10 cm in diameter was recovered from near the center of the UFG accumulation zone, which is a flat pass ~1 km wide (Naftz and others, 2002). The glacier velocity at that location was ~3.1 m a^{-1} to the northeast and decreased downslope (fig. 2 in Naftz and Smith, 1993).

In 1998, the DH98-4 borehole was logged with an acoustic televiewer to 78 m depth (Morin and others, 2000). The acoustic televiewer is a 5 cm diameter, 193 cm long instrument which is lowered into a flooded borehole on a four-conductor electric cable operated by a winch. The instrument's 500 kHz transducer rotates at 12 rps, emitting 256 acoustic pulses per revolution. Amplitude and transit time of the signal reflected off the water–ice interface are collected and used to produce a digital, magnetically oriented image of the borehole wall (Morin and others, 2000). The DH98-4 core contains particle layers, fractures and clear-ice layers inclined 10–60° from the horizontal within generally bubbly ice. The thickness, dip and strike needed to describe these features can be measured from the acoustic log just as it can from an optical borehole log (Roberson and Hubbard, 2010). The strike of a tilted plane is the compass direction of a horizontal line parallel to the plane. It is measured azimuthally from 0 to 360°. The dip is the maximum inclination of the plane, measured with respect to the horizontal. Morin and others (2000) attribute the steeply dipping (>45°) fractures in UFG DH98-4, whose strike is perpendicular to the general direction of ice movement, to extensional stress. They attribute features with shallow dip (<30°), such as particle layers or bands of clear ice, to depositional layering, which would not be tied to a strain-induced microstructure (Morin and others, 2000).

Geophysical logging instrumentation, which can include magnetic position, borehole inclination, gravity measurement, cross-hole electrical resistivity, echo sounding and optical imaging, has been used to provide detailed, oriented information on borehole geometry, englacial structure, drainage and deformation, and mass balance (Raymond, 1971; Jacobel and Raymond, 1984; Keller and others, 1995; Hubbard and others, 1998; Roberson and Hubbard, 2010). Both acoustic and optical measurements record magnetic north and produce a record of stratigraphy as a function of depth which can be used to produce an azimuthally oriented structure log. Tilted layers in the core can be matched with tilted layers in this log and used to orient the core sections that contain them. These core sections can be used to orient adjacent sections when their end faces can be matched.

Acoustic televiewers have some unique advantages in boreholes where drilling fluids are not transparent, but their resolution is only on the order of 1 mm radially and 2 mm in depth (Zemanek and others, 1970). Because the resolution of optical imaging is of the order of the wavelength (diffraction limit), optical televiewers should provide better resolution of thin stratigraphic layers and signs of foliation, and are being used increasingly by glaciologists (Hubbard and others, 2008).

We have not been able to find any previous use of stratigraphic dip and strike from the structure log to orient an ice core. This paper presents the results of a detailed microstructural analysis of 14 layers of the core from DH98-4, three of which were shallower than 78 m and contained tilted layers that could be azimuthally oriented using the structure log.

2. MEASUREMENT METHODS

2.1. Sample selection

Based on information in the UFG field notes (D.L. Naftz, http://www.usgs/gov/), we selected 14 10–50 cm long sections from the DH98-4 ice core that contained tilted features. The core was stored at –35°C at the US National Ice Core Laboratory (NICL), and samples were transported to the Ice Research Laboratory at the Thayer School of Engineering, Dartmouth College, and stored there at –25°C. The depths of the sections used for this study are shown in Table 1, along with the associated comments from the UFG field notes.

We note here that while NICL reports core lengths to the nearest millimeter, and we have also adopted this convention in our laboratory, the loss of material due to cutting and to wear or ablation in storage, along with measurement uncertainties due to surface roughness, means that there is some inherent inaccuracy of the depths reported herein. We estimate this to be on the order of 2 mm.

2.2. Grain-size measurement

We froze vertical thick sections to glass plates, reduced them (with a razor) to ~0.5 mm thin sections and photographed them on a light table between crossed polarizers. We used ImageJ digital image analysis software (Rasband, 2006) to measure the areas of 100–1200 crystals on each thin section (by drawing around each crystal and using a pixel-counting area measurement utility).

Table 1. Sample depths and their descriptions in the UFG field notes

Top m	Bottom m	Description from UFG field notes	TS	AL
42.460	42.610	BI with PL (0°)	Y	N
50.175	50.375	BI with DL (45°)	Y	Y
53.615	53.815	BI with two large particles in middle	Y	na
54.285	54.450	BI with DL (60°)	Y	Y
58.302	58.402	CI with PL	Y	na
59.126	59.305	Highly fractured ice	N	na
61.957	62.155	BI with a particle at top	Y	na
74.750	74.948	BI	Y	Y
75.312	75.412	CI (0–2 cm), BI (2–10 cm), DL (45°) at 2–8 cm.	Y	Y
93.820	94.020	BI	na	na
118.147	118.317	BI with DL (30°)	Y	na
137.607	137.707	Necking. Possible volcanic ash	Y	na
150.172	150.397	CI with BI layers (10°)	Y	na
159.272	159.400	BI and CI with interface at 10° tilt	Y	na

Notes: In the field notes, ice is described as either clear (CI) or bubbly (BI), and particle layers (PL) have larger inclusions than dirt layers (DL). The TS column indicates identification in the thick section. AL indicates identification in the acoustic log, for sections logged. Unlogged sections below 78 m, and samples with bubbles or particles but no tilted linear features, are marked na.

2.3. Crystal orientation fabric

Crystal orientation can be measured using either optical extinction or electron or X-ray diffraction techniques. Electron backscatter diffraction (EBSD) in a scanning electron microscope (SEM), which provides orientation of both *c*- and *a*-axes, was used to determine the orientation of ~100 crystals in a horizontal sample from each core section. Because a detailed fabric analysis was not performed for the UFG core, we chose to measure fabric in each of our samples, even though some did not have visible tilted layers or a corresponding acoustic log. The SEM EBSD technique is described in detail by Iliescu and others (2004) and Obbard and others (2006b). For this study, samples approximately 10 mm × 25 mm × 3 mm were cut perpendicular to the core axis, and their surfaces were shaved flat with a razor blade. Each sample was placed in a sealed container at –25°C for ~12 hours. Preferential sublimation of grain boundaries during this period allowed grains to be easily distinguished in the FEI XL-30 SEM, where the samples were held at –125 ± 5°C. Grain boundaries were identified by (a) a clear grain boundary groove and/or (b) a change in the surface etching pattern between two grains (Obbard and others, 2006a). For each grain, a representative EBSD pattern was collected. These were indexed with HKL Technology's CHANNEL 5™ software. The implied change in *c*-axis orientation due to moving the beam across the specimen is 1.07° per 2 mm traverse on the specimen, which is consistent with the typical ~1° 'orientation noise' reported by Bate and others (2005). Typically, the distance between measurements was ≤500 μm. Hence, misorientations between adjacent grains were determined to an accuracy of ~0.5°.

Because each SEM sample had <50 crystals exposed on the surface, multiple samples from approximately the same depth (4 mm apart within a 12 mm interval) were cut with the same orientation (i.e. with their long sides parallel) so that their orientation data could be plotted on the same pole figure.

2.4. Identification of dipping layers

Vertical thick sections (4 mm thick) were photographed and the angle of each tilted stratigraphic feature was measured from the horizontal. We attempted to select samples with tilted dirt or particle layers based on the core descriptions in the UFG field notes. In some cases, these turned out to be difficult to see in the quarter-cylinder core samples we received, and these samples were not usable for this analysis. For example, the dirt layer in the sample from 54.285–54.450 m was too faint for its position or angle to be measured adequately. The particle layer reported in the top 1 cm of the 58.302–58.402 m sample was not observed (instead, we found a single particle and a crack). On the other hand, a faint and previously unreported tilted layer of fine bubbles (<1 mm) in the sample from 74.750–74.948 m was observed and measured.

2.5. Acoustic televiewer log analysis

The televiewer log included amplitude and transit time as a function of depth and magnetic orientation. The log data were visualized and analyzed using WellCAD™. When a tilted plane is cut by a cylinder, and the 0–360° log section containing the resulting ellipse unrolled, the result is a sine curve. Hence, stratigraphic features in a core appear as sinusoidal bands in its unrolled log, where the width indicates layer thickness, the location of the inflection point indicates the strike direction, and dip can be calculated from the sine curve amplitude and borehole diameter. This is described in detail and well illustrated by Morin and others (2000) and Roberson and Hubbard (2010).

Many bands were visible in the acoustic log, which includes amplitude, and transit times are plotted versus depth and over 0–360°. The raw data were corrected for borehole declination (13°24′ E) and inclination (2.87°). We applied a bandpass filter to reduce the noise, with a low cut-off of 20%, a high cut-off of 80% and a filter window size of 3 × 3 data points. We fit the visually identifiable layers in the resulting image log with sinusoids and saved them with their depth data as a structure log. We identified the tilted layers found in our samples in the structure log, using their depth and dip angle, and recorded their strike.

3. RESULTS

3.1. Texture

Overall, the UFG accumulation zone core is characterized by fine-grained bubbly ice, with lenses or layers of larger-grained clear ice that range in thickness from a few millimeters to 10 cm. Vertical thin sections of 2 cm high sections of each sample are shown in Figure 1. In samples from above 150 m, the mean grain size was 0.9–10.9 mm^2, with an average value of 3.4 mm^2. Overall, the grain size was not correlated with the presence of dirt or particles and there was no statistically significant increase in grain size with age. This is not surprising given the relatively young age of the core (215 years) and the likely migration recrystallization taking place (discussed in section 4).

3.2. Identification of tilted layers

The clear-ice layers and layers of dirt and particles are often inclined 10–60° from the horizontal. The most pronounced of these in samples we studied are shown in both thick and corresponding thin sections in Figure 2.

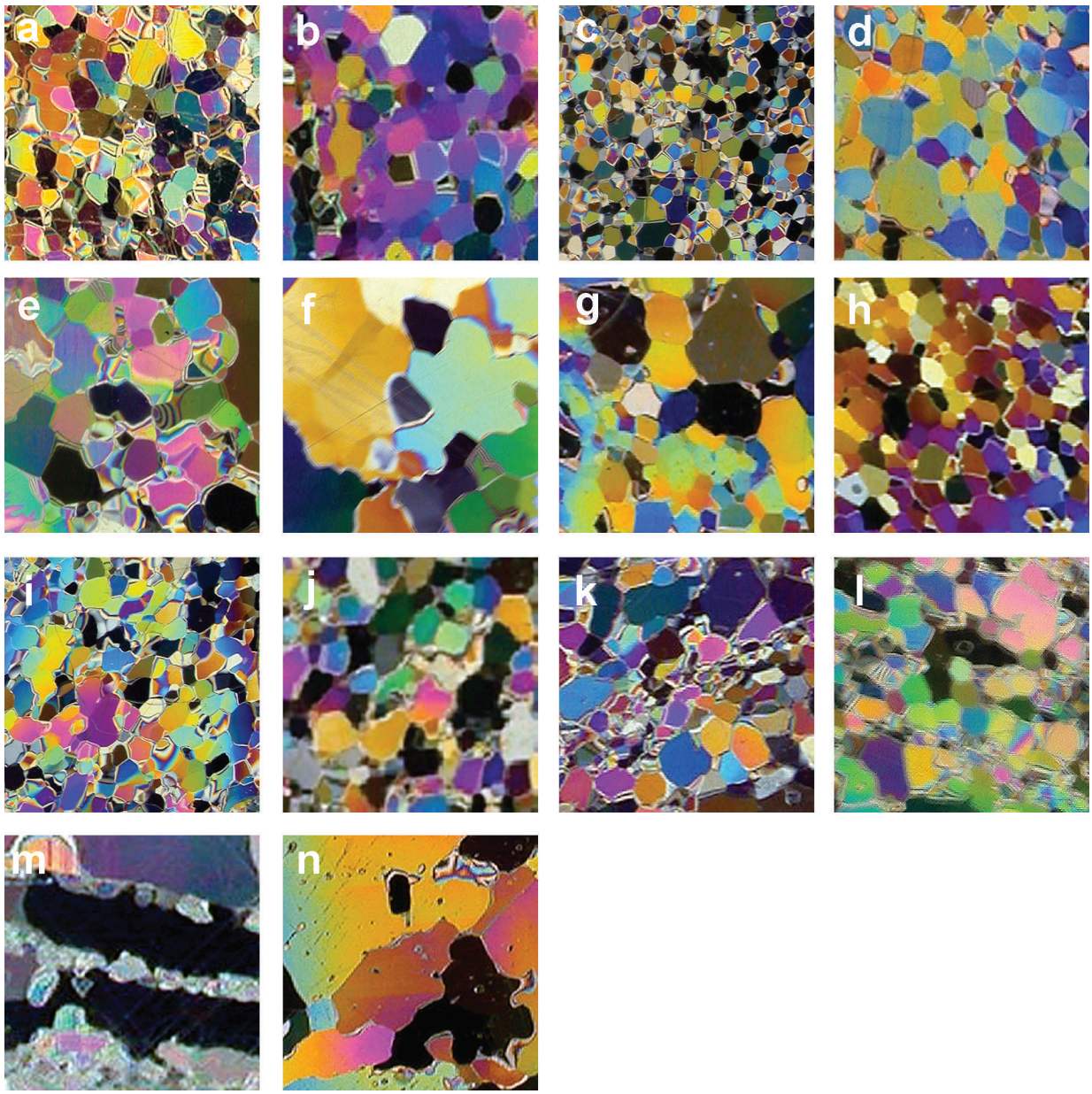

Fig. 1. Vertical thin sections. Two-centimetre square portions of each with depth at top of image and mean grain size of the entire sample: (a) 42.515 m (2.0 mm^2); (b) 50.182 m (3.4 mm^2); (c) 53.752 m (0.9 mm^2); (d) 54.364 m (4.4 mm^2); (e) 58.345 m (5.1 mm^2); (f) 59.257 m (10.9 mm^2); (g) 61.992 m (2.6 mm^2); (h) 74.808 m (3.1 mm^2); (i) 75.382 m (1.5 mm^2); (j) 93.820 m (3.3 mm^2); (k) 118.239 m (5.3 mm^2); (l) 137.662 m (5.6 mm^2); (m) 150.336 m (115.0 mm^2); and (n) 159.354 m (36.8 mm^2).

The sample from 50.175–50.375 m (part shown in Fig. 2a) was bubbly ice with a mean grain size of 3.4 mm^2. It contained a 7 mm thick layer of bubble-free ice with larger grains (~50 mm^2), and a dirt layer immediately underneath this. In quarter cross-section samples, the dirt or particle layers are exposed on the two cut faces. The azimuthal relationship of the (arbitrary) vertical sectioning to the strike of a tilted layer within determines the projection of the layer on each face. The dip of a tilted layer can be determined from its angle on the two cut faces and the fact that the angle between these faces is 90°. The dip of the clear-ice (and dirt) layer in the sample from 50.175–50.375 m was found to be 36°. The sample from 74.750–74.948 m (mean grain size 3.1 mm^2) contained a tilted layer of fine bubbles that was easy to see in the whole quarter-core section but is hard to see in Figure 2b and is indicated by arrows. The dip of this layer was 58°. The sample from 75.312–75.412 m (mean grain size 1.5 mm^2) contained a dirt layer (Fig. 2c) with a dip of 42°. Some other samples had dirt or clear-ice layers that were nominally horizontal and so not useful for azimuthal orientation (54.285–54.450, 58.302–58.402 and 61.957–62.155 m), or had easily measured dipping layers but were from sections deeper than the logging (118.147–118.317 and 150.172–150.397 m).

In the two deepest samples (150.172–150.397 and 159.272–159.400 m), shear planes were observed (Fig. 2m), where fractures have displaced large grains and provided a location for the nucleation of new (~1 mm) grains.

3.3. Crystal orientation fabric

Contoured equal-area projection upper-hemisphere pole figures were produced for all but the two deepest samples (where grain size was too large to sample more than a few

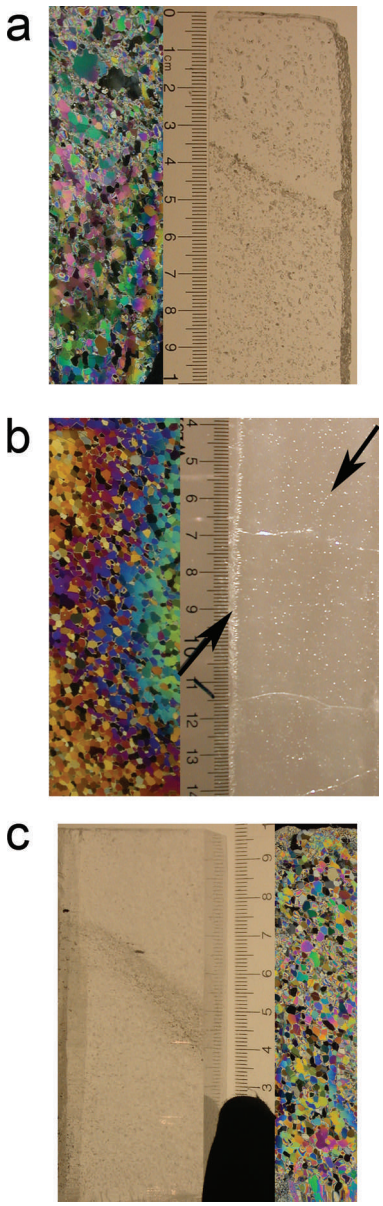

Fig. 2. Thick (5–10 mm) and thin (0.5 mm) sections: (a) 50.175–50.275 m, with a clear-ice layer, dip 36°; (b) 74.750–74.850 m, with a fine bubble line (possibly a healed crack), dip 58°; (c) 75.312–75.412 m, with a particle layer, dip 42°. The images are oriented as they were in the core.

grains). In each case, the crystal orientation fabric was either single- or multiple-maximum, with the latter having two, three or four maxima. The pole figures for the samples from Figure 1 are shown in Figure 3. The center of each pole figure corresponds to the core axis. Each crystal is represented by one point on the *c*-axis {0001} pole figure, which identifies the normal to the basal plane, and three corresponding points (90° from the {0001} pole and from one another) on the *a*-axis {11–20} pole figure. The pole figures are contoured for densities of 2–10% in 2% intervals. In the first *c*-axis pole figure, for example, 20% of points fall in 2% of the pole figure. Ideally for fabric analysis we would like orientations from 100–200 different crystals at each depth. Because grain size was sometimes large compared with the small available sample size, we measured only 71–138 separate crystals per sample. This makes it more difficult to accurately interpret crystal orientation fabric from these pole figures.

Note that the lack of azimuthal orientation of the core sections when they were removed from the borehole would normally prevent one from making meaningful comparisons between the crystal orientation fabric measured in samples from different sections and overall glacier movement. Because we were able to correlate foliation seen in our samples with the same layers in the structure log, however, we can make this comparison. For the three samples of interest with identifiable tilted layers measured as described in section 3.2, the normals to these tilted planes have been superimposed on the {0001} pole figures in Figure 3b, h and i and are indicated by red stars. The accuracy of measurement of the orientation of the tilted planes is estimated to be 2°, based on the manual tilt-angle measurement procedure using thick sections.

3.4. Acoustic televiewer log analysis

A section of the structure log is shown in Figure 4. The amplitude and transit time of the acoustic waves are presented as planar projections of the cylindrical borehole, with azimuth shown at the top. Horizontal layers which intersect the borehole are horizontal lines on the structure log. Tilted layers produce a sinusoidal pattern. These are fitted manually with a sinusoid, the amplitude and shift of which reflect the dip and strike of the tilted layer. We fitted every identifiable layer, including horizontal ones, producing in WellCAD™ a table of stratigraphic features that could be compared to the core description in the field notes and to the samples themselves.

Acoustic impedance contrast between ice and water is poor, and detailed structural features were difficult to accurately fit in the borehole log, even after the low-pass filter was applied. The accuracy of this technique is limited more by the user's ability to pick out and accurately fit the features than by the resolution of the instrument. By varying the position of the sinusoids drawn, for this dataset we estimate it to be 20° in azimuth and 10° in dip. Nonetheless, we were able to confirm that the acoustic log contained some of the same features seen in the core, specifically the 7 mm thick clear-ice layer at 50.205–50.226 m (Fig. 2a) and the ~10 mm thick particle layer at 75.334–75.364 m (Fig. 2c). On the structure log, these features appear at 50.15 and 75.25 m, with the differences in depth probably due to slight errors in the core archiving or logging processes. The difference in thickness of the features between the core and log (they are 7 and 10 mm thick in the core but 3 and 80 mm thick in the log) is probably due to the amount of noise in the log, or to the possibility that the layer thickness in the core sample we had was not representative of the average thickness of that layer or was affected by other layers in the acoustic sampling region.

4. INTERPRETATION AND DISCUSSION

The predominantly straight grain boundaries and equiaxed grains in most of the samples from 42.460–137.807 m suggest normal grain growth. The samples from 59.126–59.305 m (Fig. 1f), 150.172–150.397 m (Fig. 2m) and 159.272–159.400 m (Fig. 2n), on the other hand, had larger, interlocking grains (10.9, 115.0 and 36.8 mm^2, respectively) with tortuous grain boundaries suggesting abnormal grain growth (Alley, 1988).

Deep in glaciers and ice sheets where there is high strain energy and temperatures higher than –10°C, strain-induced

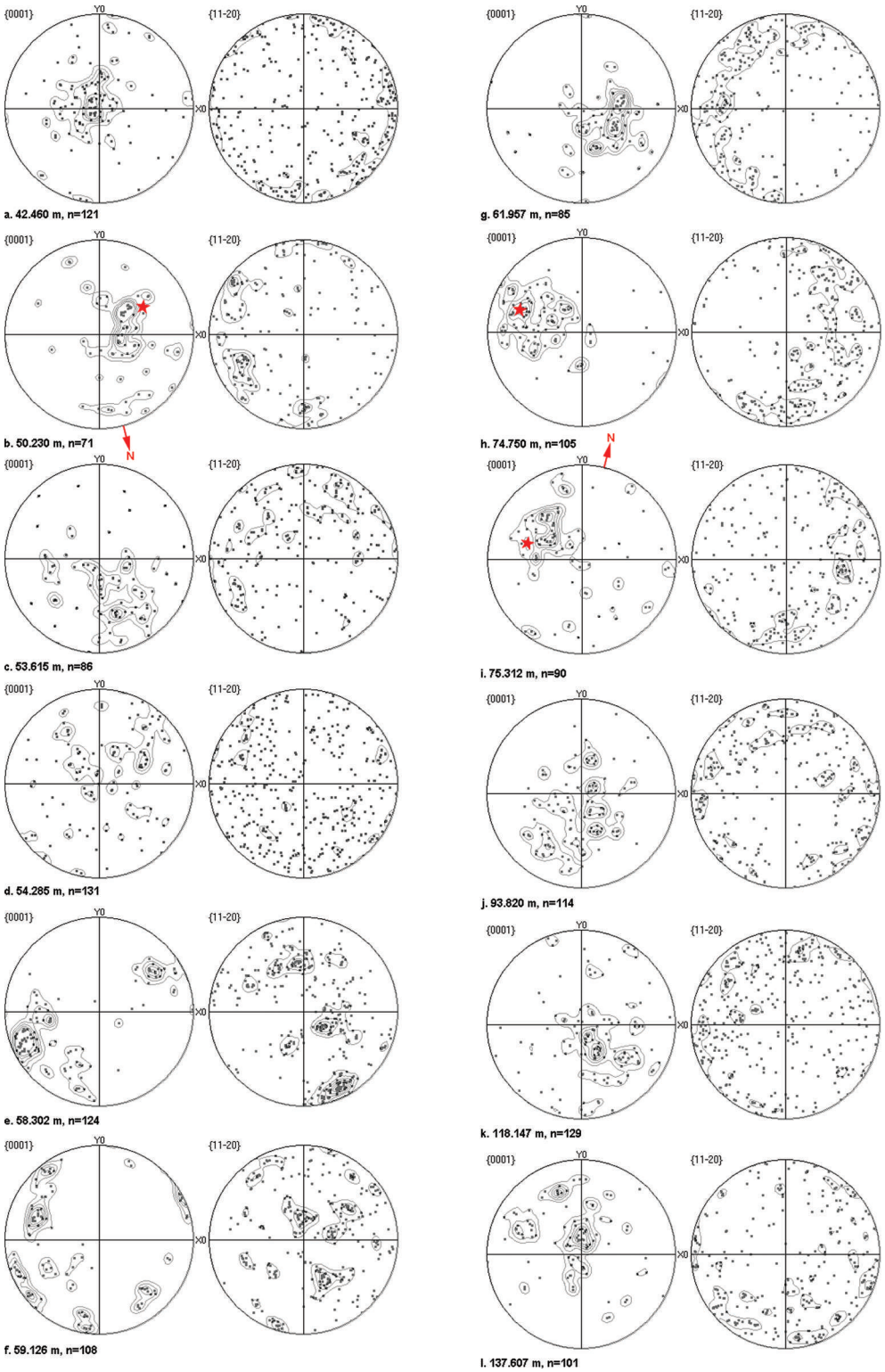

Fig. 3. Contoured equal-area projection upper-hemisphere pole figures from all samples. The normals to the tilted planes (identified with red stars) have been superimposed on the {0001} pole figures in (b) 50.230 m, (h) 74.750 m and (i) 75.312 m.

boundary migration (SIBM) or migration recrystallization produces a mixture of large and small grains and tortuous or interlocking grain boundaries (Matsuda and Wakahama, 1978; Alley, 1988; Duval and Castelnau, 1995). SIBM takes place when grain boundaries in strained (high dislocation density) grains move away from their center of curvature, producing a microstructure with irregular, interlocking grains. When parts of these are cut off by grain boundary migration, a new strain-free grain is nucleated and a cross section reveals a mixture of large grains and multiple smaller grains with similar orientations. This process produces a bimodal grain-size distribution, and reintroduces a more random fabric (Duval and Castelnau, 1995; Gow and others, 1997; Thorsteinsson and others, 1997). At UFG, the mean annual surface air temperature is –6.9°C and the temperature at 10 m depth is 0 ± 0.4°C (Naftz and others, 2002). Hence, migration recrystallization, which would produce the mixture of large and small grains seen in Figure 1, is possible at

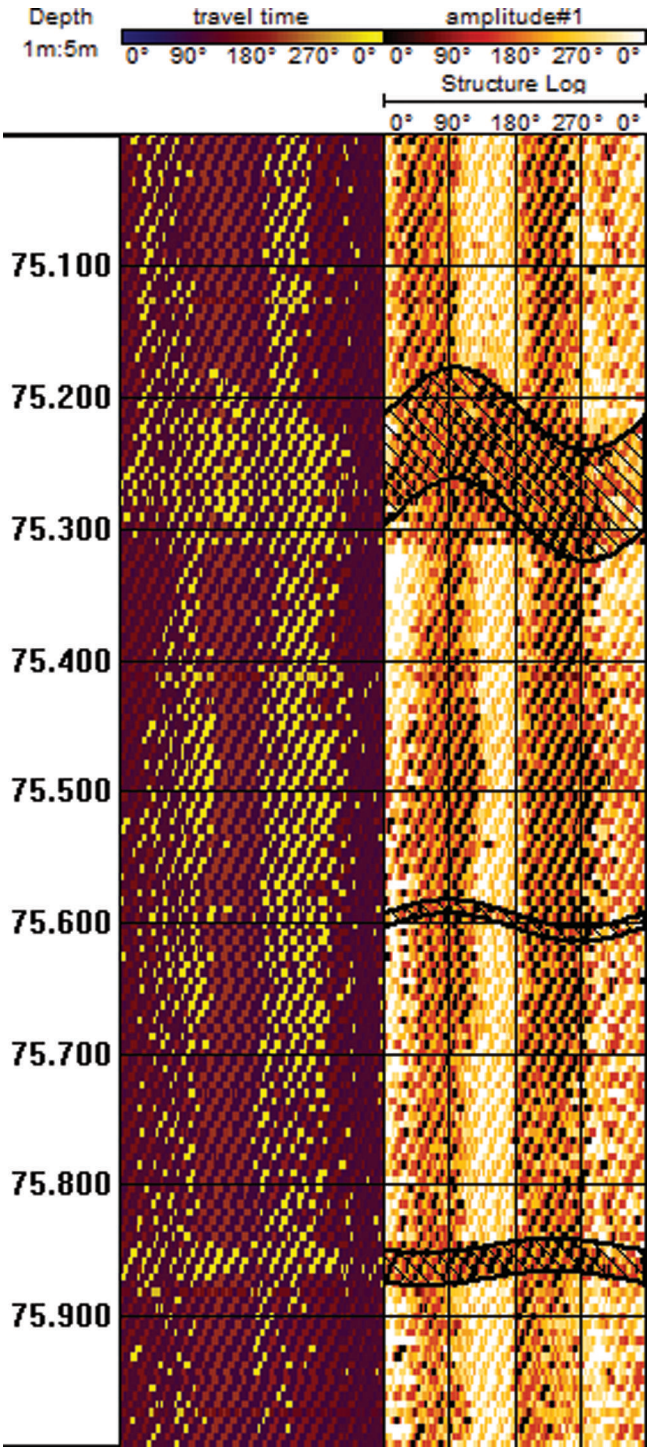

Fig. 4. A section of the acoustic log (transit time and amplitude) filtered as described in the text, with features of interest indicated with sinusoidal bands on the superimposed structure log.

all depths and may explain the mix of grain sizes in Figure 1e, f, g and k. Further, our two deepest UFG samples (150.172–150.397 and 159.272–159.400 m) contained clear slip layers (Fig 1m), where large grains are separated by planes of very small grains, which are probably shear bands.

Parts of the 58.302–58.402 m sample, the entire 59.126–59.305 m sample and the 7 mm thick layer seen in the 50.175–50.375 m sample (Fig. 2a) were bubble-free with relatively large grain size. Bubble-free ice can be the result of melting and refreezing, during exposure to warmer temperatures for instance. The overall warm temperatures in this temperate glacier could be expected to lead to grain boundary migration and the associated large grains and tortuous grain boundaries. However, slow refreezing of semi-melted layers can also contribute to larger grain size.

Despite the limitations imposed by small sample size, the crystal orientation fabrics shown in Figure 3 are informative. While the *c*-axes generally form broad, sub-vertical clusters, the *a*-axes show more variation. They are generally scattered in the sub-horizontal plane (i.e. perpendicular to the *c*-axes), but in some cases are themselves found in clusters (Fig. 3b, e and f). The samples from 50.230 m (Fig. 3b) and 58.302 m (Fig. 3e) each have a broad sub-vertical cluster of *c*-axes and three broad clusters of *a*-axes. This combination suggests a single crystal, perhaps sampled repeatedly. However, in Figure 1b (50.182–50.202 m) we see many, relatively small (3.4 mm^2) crystals. Hence this is simply a strongly aligned fabric. While the sample from 58.302 m has the same *c*-axis fabric, it was clear ice with a mixture of large and small grains. The clusters in Figure 3e may therefore represent repeated sampling (in several EBSD samples) of the same grains. In the sample from 59.126–59.305 m, the combination of tortuous grain boundaries (Fig. 1f) and *c*-axis clusters with shared *a*-axes suggests a few large interlocking grains sampled in different locations. The mean grain size of 10.9 mm^2 supports this. This layer, which was entirely bubble-free, may be the result of a summer surface melt.

Our multiple-maxima fabrics were not arranged in a diamond pattern as in Emmons Glacier (Rigsby, 1951), but this may be because our samples came from depth, rather than the surface, and probably had complex deformational histories.

In summary, the crystal orientation fabric in the different layers of the core alternates between three basic types. The first and predominant type is found at 42.480, 53.615, 61.957, 74.750, 75.312, 93.820 and 137.807 m, where the *c*-axes fall in a sub-vertical cluster and the *a*-axes are scattered at 90° to them. This is consistent with slip on the {0001} plane in the {11–20} direction, due to compression along a nominally vertical axis. The second type is found at 58.302 and 59.126 m, where there are both *c*-axis and *a*-axis clusters. These samples included clear ice and a mix of large and small grains and some irregular grain boundaries (Fig. 1e and f). They have probably been affected by SIBM. The fabric of the 50.230 m sample falls somewhere between these. The third fabric type is pseudo-random, with somewhat more scattered *c*- and *a*-axis normals (54.285 and 118.147 m). Both these samples are bubbly ice with a mixture of large and small grains with straight grain boundaries. The fabric could be a remnant of the original random fabric that existed following deposition, or be due to the nucleation of the new (small) grains.

Note that because EBSD produces full orientation information, it enables us to differentiate between microstructures possessing the same *c*-axis fabric but different *a*-axis fabrics. A *c*-axis cluster associated with scattered *a*-axes represents a strongly aligned crystal orientation fabric stemming from uniaxial compression, while a *c*-axis cluster associated with clustered *a*-axes represents SIBM.

The dirt layer in Figure 2a corresponds with one recorded at 50.195–50.260 m in the UFG field notes, with a reported dip of 45°. The particle layer in Figure 2c corresponds to that recorded at 75.332–75.392 m in the UFG field notes, also with a reported dip of 45°. The tilted bubble layer, possibly a healed crack, in the sample from 74.750–74.850 m (Fig. 2b),

is not recorded in the UFG field notes and was too fine for the acoustic televiewer to distinguish. Normals to the tilted features shown in Figure 2a–c are shown in the corresponding pole figures in Figure 3b, h and i (red stars).

In the field notes, dip angles were recorded as either 10°, 30°, 45° or 60°, with no intermediate values used, so the dip angles measured here, of 36° and 42° for the samples shown in Figure 2a and c, respectively, are reasonable actual dips for these features. In the WellCAD™ structure log, the first (at a log depth of 50.15 m) has a dip of 26.6° (and a strike of 250.2° from north). The last, at a log depth of 75.25 m, has a dip of 33.2° (and a strike of 271.8° from north). The differences between dip measured in the core sections and that measured on the structure log are most likely due to the poor resolution of the acoustic log.

Both features strike 250–272° from north, or approximately perpendicular to the flow direction. Hence these tilted layers are probably from large-scale stress-related foliation, rather than local irregularities in the depositional surface. Their plane normals (red stars in Fig. 3) are approximately coincident with the *c*-axis maxima, supporting our hypothesis of slip on the basal plane. Finally, the strike of these features can be used to orient the pole figures in Figure 3b and i.

5. CONCLUSIONS

It has long been recognized that borehole logging provides a record of stratigraphy, and the usefulness of optical televiewing for investigating englacial ice and debris structures exposed at the surface has recently been demonstrated (Roberson and Hubbard, 2010). The present work shows that borehole logging also presents the opportunity to orient core sections containing dipping features, so that we may compare their crystal orientation fabric to flow direction, bedrock topography, etc. With this new approach, we can perform comprehensive flowline and microstructural studies of deep ice in the accumulation zone of temperate glaciers that contains visible tilted foliation that will help us to better understand the connections between glacier dynamics and microstructure. EBSD fabric analysis, with its *c*- and *a*-axis information, has proven useful in our examination of microstructure in the UFG, allowing us to distinguish between two types of crystal orientation fabric possessing clusters of {0001} poles. The difference was illustrated quite clearly by the parallel use of thin sections, and together the two techniques reveal a microstructure produced by vertical compression and strain-induced boundary migration in this relatively warm temperate zone glacier.

Higher-resolution logs (with better impedance contrast) than described here are needed to achieve more accurate results. We expect that the improvements in and increased use of borehole logging techniques will enable glaciologists to orient more ice cores. This capability will contribute to the study of the relationship between glacier and ice-sheet flow, deformation and microstructure, and the correct interpretation of climate information stored in the ice-core record.

ACKNOWLEDGEMENTS

We thank R. Morin, D. Naftz and P. Schuster of the US Geological Survey for the field log, acoustic data and their advice, and G. Lloyd of the Institute of Geophysics and Tectonics, University of Leeds, UK. We are grateful for the detailed comments of A. Treverrow and two anonymous reviewers. This work was funded under US National Science Foundation (NSF) grant OPP-0738975 and the Dartmouth Women in Science Project. The views and conclusions contained herein are those of the authors and should not be interpreted as necessarily representing official policies, either expressed or implied, of the NSF or the US Government.

REFERENCES

Alley, R.B. 1988. Fabrics in polar ice sheets: development and prediction. *Science,* **240**(4851), 493–495.

Bate, P.S., R.D. Knutsen, I. Brough and F.J. Humphreys. 2005. The characterization of low-angle boundaries by EBSD. *J. Microsc.,* **220**(1), 36–46.

Budd, W.F. 1972. The development of crystal orientation fabrics in moving ice. *Z. Gletscherkd. Glazialgeol.,* **8**(1–2), 65–105.

Budd, W.F. and T.H. Jacka. 1989. A review of ice rheology for ice sheet modelling. *Cold Reg. Sci. Technol.,* **16**(2), 107–144.

Budd, W.F. and M. Matsuda. 1974. On preferred orientation of polycrystalline ice by biaxial creep. *Low Temp. Sci., Ser. A* 32, 261–265. [In Japanese with English summary.]

Duval, P. and O. Castelnau. 1995. Dynamic recrystallization of ice in polar ice sheets. *J. Phys. IV [Paris],* **5**(C3), 197–205.

Gow, A.J. and D.A. Meese. 2007. Physical properties, crystalline textures and *c*-axis fabrics of the Siple Dome (Antarctica) ice core. *J. Glaciol.,* **53**(183), 573–584.

Gow, A.J. *and 6 others*. 1997. Physical and structural properties of the Greenland Ice Sheet Project 2 ice cores: a review. *J. Geophys. Res.,* **102**(C12), 26,559–26,575.

Hambrey, M.J. 1976. Debris, bubble, and crystal fabric characteristics of foliated glacier ice, Charles Rabots Bre, Okstindan, Norway. *Arct. Alp. Res.,* **8**(1), 49–60.

Hambrey, M.J. 1977. Foliation, minor folds and strain in glacier ice. *Tectonophysics,* **39**(1–3), 397–416.

Hubbard, B., A. Binley, L. Slater, R. Middleton and B. Kulessa. 1998. Inter-borehole electrical resistivity imaging of englacial drainage. *J. Glaciol.,* **44**(147), 429–434.

Hubbard, B., S. Roberson, D. Samyn and D. Merton-Lyn. 2008. Digital optical televiewing of ice boreholes. *J. Glaciol.,* **54**(188), 823–830.

Iliescu, D., I. Baker and H. Chang. 2004. Determining the orientations of ice crystals using electron backscatter patterns. *Microsc. Res. Techn.,* **63**(4), 183–187.

Jacobel, R. and C. Raymond. 1984. Radio echo-sounding studies of englacial water movement in Variegated Glacier, Alaska. *J. Glaciol.,* **30**(104), 22–29.

Jonsson, S. 1970. Structural studies of subpolar glacier ice. *Geogr. Ann.,* **52A**(2), 129–145.

Kamb, B. 1972. Experimental recrystallization of ice under stress. *In* Heard, H.C., I.Y. Borg, N.L. Carter and C.B. Raleigh, *eds. Flow and fracture of rocks*. Washington, DC, American Geophysical Union, 211–241. (Geophysical Monograph 16.)

Kang, S. *and 7 others*. 2002. Glaciochemical records from a Mt. Everest ice core: relationship to atmospheric circulation over Asia. *Atmos. Environ.,* **36**(21), 3351–3361.

Keller, K., N. Gundestrup, D. Dahl-Jensen, C.C. Tscherning, R. Forsberg and S. Ekholm. 1995. The ice deformation and mass balance at the summit of Greenland as determined by GPS and gravity measurements. *In* Obleitner, F. and O.B. Olesen, *eds. Mass-balance and related topics of the Greenland ice sheet*. Copenhagen, Grønlands Geologiske Undersøgelse, 15–18. (Open File Series 95/5.)

Matsuda, M. and G. Wakahama. 1978. Crystallographic structure of polycrystalline ice. *J. Glaciol.,* **21**(85), 607–620.

Mayewski, P.A., W.B. Lyons, N. Ahmad, G. Smith and M. Pourchet. 1984. Interpretation of the chemical and physical time-series retrieved from Sentik Glacier, Ladakh Himalaya, India. *J. Glaciol.,* **30**(104), 66–76.

Morin, R.H., G.E. Descamps and L.D. Cecil. 2000. Characterizing englacial structure from analysis of acoustic televiewer logs, Upper Fremont Glacier, Wyoming. *In Proceedings of the Seventh International Symposium on Mineral and GeoTechnical Logging, 24–26 October 2000, Golden, Colorado*. Houston, TX, Society of Petrophysicists & Well Log Analysts. Minerals and Geotechnical Logging Society, 235–243.

Naftz, D.L. and M.E. Smith. 1993. Ice thickness, ablation, and other glaciological measurements on Upper Fremont Glacier, Wyoming. *Phys. Geogr.,* **14**(4), 404–414.

Naftz, D.L. *and 7 others*. 1996. Little Ice Age evidence from a south-central North American ice core, U.S.A. *Arct. Alp. Res.,* **28**(1), 35–41.

Naftz, D.L. *and 6 others*. 2002. Ice core evidence of rapid air temperature increases since 1960 in alpine areas of the Wind River Range, Wyoming, United States. *J. Geophys. Res.,* **107**(D13), 4171. (10.1029/2001JD000621.)

Obbard, R., I. Baker and D. Iliescu. 2006a. Correspondence. Grain boundary grooving in ice in a scanning electron microscope. *J. Glaciol.,* **52**(176), 169–172.

Obbard, R., I. Baker and K. Sieg. 2006b. Using electron backscatter diffraction patterns to examine recrystallization in polar ice sheets. *J. Glaciol.,* **52**(179), 546–557.

Rasband, W.S. 2006. *ImageJ program.* Bethesda, MA, National Institutes of Health.

Raymond, C.F. 1971. Flow in a transverse section of Athabasca Glacier, Alberta, Canada. *J. Glaciol.,* **10**(58), 55–84.

Rigsby, G.P. 1951. Crystal fabric studies on Emmons Glacier, Mount Rainier, Washington. *J. Geol.,* **59**(6), 590–598.

Roberson, S. and B. Hubbard. 2010. Application of borehole optical televiewing to investigating the 3-D structure of glaciers: implications for the formation of longitudinal debris ridges, midre Lovénbreen, Svalbard. *J. Glaciol.,* **56**(195), 143–156.

Schuster, P.F., D.E. White, D.L. Naftz and L.D. Cecil. 2000. Chronological refinement of an ice core record at Upper Fremont Glacier in south central North America. *J. Geophys. Res.,* **105**(D4), 4657–4666.

Thorsteinsson, T., J. Kipfstuhl and H. Miller. 1997. Textures and fabrics in the GRIP ice core. *J. Geophys. Res.,* **102**(C12), 26,583–26,599.

Thorsteinsson, T., E.D. Waddington and R.C. Fletcher. 2003. Spatial and temporal scales of anisotropic effects in ice-sheet flow. *Ann. Glaciol.,* **37**, 40–48.

Zemanek, J., E.E. Glenn, L.J. Norton and R.L. Caldwell. 1970. Formation evaluation by inspection with the borehole televiewer. *Geophysics,* **35**(2), 254–269.

MS received 23 August 2010 and accepted in revised form 30 June 2011